

ON THE HALO OCCUPATION OF DARK BARYONS

JEREMY L. TINKER & HSIAO-WEN CHEN

Kavli Institute for Cosmological Physics & Department of Astronomy and Astrophysics, University of Chicago
Draft version October 25, 2018

ABSTRACT

We introduce a new technique that adopts the halo occupation framework for understanding the origin of QSO absorption-line systems. Our initial study focuses specifically on Mg II absorbers. We construct a model of the gaseous content in which the absorption equivalent width W_r is determined by the amount of cold gas, in the form of discrete clouds, along a sightline through a halo. The two quantities that we specify per halo in the model are (1) the mean absorption strength per unit surface mass density $A_W(M)$, and (2) the mean covering factor $\kappa_g(M)$ of the gaseous clouds. These parameters determine the conditional probability distribution of W_r as a function of halo mass, $P(W_r|M)$. Two empirical measurements are applied to constrain the model: (i) the absorber frequency distribution function and (ii) the W_r -dependent clustering amplitude. We find that the data demand a rapid transition in the gas content of halos at $\sim 10^{11.5} h^{-1} M_\odot$, below which halos contain predominantly cold gas and beyond which gas becomes predominantly hot. In order to reproduce the observed overall strong clustering of the absorbers and the anti-correlation between W_r and halo mass M , roughly 5% of gas in halos up to $10^{14} h^{-1} M_\odot$ is required to be cold. The gas covering factor is near unity over a wide range of halo mass, supporting that Mg II systems probe an unbiased sample of typical galaxies. We discuss the implications of our study in the contexts of mass assembly of distant galaxies and the origin of QSO absorption line systems.

Subject headings: Cosmology: theory — dark matter halos — quasars: absorption lines — galaxies: evolution

1. INTRODUCTION

The forest of Ly α absorption line systems observed in the spectra of background QSOs is a sensitive probe of intervening baryonic matter that is otherwise invisible (see Rauch 1998 for a comprehensive review). The gaseous clouds uncovered by these absorption features span a wide range of ionization state and neutral hydrogen column density over $N(\text{H I}) = 10^{12} - 10^{22} \text{ cm}^{-2}$ and are understood to originate in a range of environments in the dark matter distribution, from moderate overdensities to fully collapsed structures (e.g. Davé et al. 1999). Strong Ly α absorbers with $N(\text{H I}) \gtrsim 2 \times 10^{20} \text{ cm}^{-2}$ are thought to be the high-redshift analogue to present-day galaxies (Wolfe et al. 2005). Studies of these high-density neutral gas clouds show that they all contain low ions such as Si⁺, Fe⁺, and Mg⁺ (e.g. Lu & Wolfe 1994; Prochaska et al. 2003). Conversely, studies indicate that Mg II absorbers of rest-frame absorption equivalent width $W_r(2796) \geq 0.3 \text{ \AA}$ arise in gaseous clouds of $N(\text{H I}) = 10^{18} - 10^{22} \text{ cm}^{-2}$ (Churchill et al. 2000; Rao et al. 2006). Over the redshift range $z = 0.35 - 2.5$, the Mg II $\lambda\lambda 2796, 2803$ doublet transitions are shifted to the optical spectral range $\lambda_{\text{obs}} = 3800 - 10,000 \text{ \AA}$ and therefore provide a convenient optical probe of dark baryons in extended gaseous halos of typical galaxies along random lines of sight.

Extensive studies of the physical properties of Mg II absorbers have been carried out by various authors. Early studies that compared abundance ratios between different ions associated with Mg II absorbers showed that these absorbers arise in photo-ionized gas of temperature $T \sim 10^4 \text{ K}$ (e.g. Bergeron & Stasinska 1986; Hamann 1997). In addition, high-resolution spectra of strong absorbers also show that these systems are multi-component, with W_r roughly proportional to the number of components in the system (Petitjean & Bergeron 1990; Churchill & Vogt 2001; Prochter et al. 2006). Finally, comparisons of galaxies and

Mg II absorbers along common lines of sight also indicate that Mg II absorbers at $\langle z \rangle = 0.65$ are associated with luminous galaxies (Bergeron 1986; Steidel et al. 1994) and that field galaxies possess extended gaseous halos to projected distances of $r \approx 50 h^{-1} \text{ kpc}$ (Lanzetta & Bowen 1990; Steidel 1993).

Extended halos of cool gas around galaxies were predicted by Spitzer (1956) and discussed in more detail in Bahcall & Spitzer (1969). Theoretical models that explain the origin of extended gaseous halos around galaxies include (i) the stripping of gas from the accretion of small, gas-rich satellites into a larger system (Wang 1993); (ii) cold gas gravitationally bound to small-scale substructure within the dark matter halo (e.g., Sternberg et al. 2002); and (iii) a two-phase medium, cold clouds condense out of a hotter halo through thermal instability (Mo & Miralda-Escude 1996; Maller & Bullock 2004; Chelouche et al. 2007). These models imply that W_r reflects the potential well of the dark matter halo—more massive systems sustain bigger gaseous halos with a higher velocity dispersion.

However, recent studies have yielded conflicting results that challenge this classical picture. While some authors present observations that suggest strong Mg II absorbers originate primarily in galactic superwinds from low-mass galaxies (Prochter et al. 2006; Bouché et al. 2006; Murphy et al. 2007), others show that Mg II absorbing galaxies resemble typical field galaxies (Zibetti et al. 2005; Kacprzak et al. 2007; Nestor et al. 2007) and the covering fraction of Mg⁺ ions is roughly 50% (Tripp & Bowen 2005). A particularly puzzling result is the anti-correlation between $W_r(2796)$ (hereafter W_r) and clustering amplitude by Bouché et al. (2006) (hereafter B06). These authors measured the cross-correlation function of Mg II absorbers and luminous red galaxies (LRGs) in data release three of the Sloan Digital Sky Survey (SDSS DR3; Abazajian 2005). From the relative bias with respect to LRGs, B06 inferred the mean halo mass of absorbers as a

function of W_r , finding that strong absorbers of $W_r = 2 - 2.85 \text{ \AA}$ on average arise in less massive dark matter halos of $\langle \log M \rangle = 11.11$, while absorbers of $W_r = 0.3 - 1.15 \text{ \AA}$ on average arise in dark matter halos of $\langle \log M \rangle = 12.49$. The authors consider this anti-correlation in strong favor of a superwind origin for $W_r > 1 \text{ \AA}$ absorbers; the large equivalent width in low-mass systems is attributed to the outflow velocity of the systems undergoing starburst episodes.

The cross-correlation function of absorbers and galaxies on large scales ($\gtrsim 1 h^{-1} \text{ Mpc}$) provides a quantitative characterization of the origin of these absorbers. The clustering of absorbers is a consequence of the halos in which they are found. Low-mass halos form in a wide range of environments while high-mass halos can only form in the most dense regions of the dark matter distribution, thus high-mass halos are highly clustered. The clustering of halos depends only on simple gravitational physics, and the bias of dark matter halos as a function of mass is a well-established relation in the standard CDM cosmology. Thus it is straightforward to infer a mean halo mass from large-scale clustering, as presented in B06.

However, when interpreting the clustering of gaseous clouds based on the presence of a specific ion, it is necessary to consider the state of the gas in the dark matter halos. For example, if the observed Mg^+ ions originate in photo-ionized gas of temperature $T \sim 10^4 \text{ K}$, then the observed anti-correlation between W_r and $\langle M \rangle$ may be produced when the halo gas in massive dark matter halos becomes too hot for abundant Mg^+ to survive. To investigate how the content of warm/cold gas depends on halo mass, we introduce a new technique that adopts the halo occupation framework for studying the origin of Mg II absorbers. This same technique can also be applied for studying the nature of QSO absorption-line systems.

Our halo occupation approach is similar to the Halo Occupation Distribution (HOD) method that was developed to establish an empirical mapping between galaxies and dark matter halos (e.g., Seljak 2000; Scoccimarro et al. 2001; Berlind & Weinberg 2002; see Zheng & Weinberg 2007 and references therein). This mapping is purely statistical in nature; it interprets galaxy bias based on the probability that a halo of mass M contains N galaxies of a given class, $P(N|M)$. The probability, $P(N|M)$, is constrained by measurements of the space density of the class of objects and their two-point auto-correlation function. HOD analysis of galaxy clustering data can provide insight into galaxy formation and evolution (van den Bosch et al. 2003b; Cooray 2006; Zheng et al. 2007; White et al. 2007; Tinker et al. 2007) and to constrain cosmological parameters (van den Bosch et al. 2003a, 2007; Tinker et al. 2005; Tinker 2007; Zheng & Weinberg 2007). In this paper, we extend this framework to characterize the cold gas detected through QSO absorption lines and focus specifically on Mg II absorbers.

To study the dark matter halo population of Mg II absorbers, we adopt a conditional probability distribution of equivalent widths $P(W_r|M)$ to describe the halo occupation of cold gas. Our technique is fundamentally the same as the conditional luminosity function for interpreting galaxy bias (Yang et al. 2003; van den Bosch et al. 2007). In our approach, we choose to parameterize $P(W_r|M)$ —the distribution of W_r within a halo of given mass—according to expectations of a uniform gaseous halo, in which the equivalent width is proportional to the density-weighted path-length along a sight-line through the halo. The parameters of $P(W_r|M)$ are left free and con-

strained by empirical data. The available observations are (1) the frequency distribution function $d^2N/(dW_r dz)$, the number density of absorbers per unit absorption equivalent width interval per unit redshift path, and (2) the large-scale bias relative to LRGs. The halo occupation analysis allows us to go beyond simply estimating the mean mass of dark matter halos that host absorbers and constrain the distribution of these halos as a function of W_r .

We will consider two scenarios for $P(W_r|M)$. In the first scenario, the fraction of cold gas relative to dark matter mass is a smoothly varying function of halo mass. This scenario is motivated by the canonical model for halo gas in which accreting gas is always shock-heated to the virial temperature when it crosses the virial radius (e.g., White & Frenk 1991). The gas then cools from the inside out, creating a cooling radius that varies with the properties of the halo. We will demonstrate that this model cannot simultaneously fit the frequency and bias data; models of this type that reproduce the frequency distribution predict a positive correlation between W_r and M because more massive halos are expected to contain more absorbing gas. Taking into account the fact that the Mg II transitions probe primarily warm, photo-ionized gas, we include in the second model a transitional mass scale, at which shock heated gas progressively takes over higher mass halos and the absorption efficiency is significantly reduced. In the transition region between entirely ‘cold-mode’ and ‘hot-mode’ halos, heating occurs as an *inside-out* process. Namely, a highly ionized core expands until it envelops the entire gas halo (e.g., Dekel & Birnboim 2006). We allow the mass scale and width of this transition to be free parameters. In addition, we allow some fraction of cold gas in the hot halos that is also constrained by empirical data. We demonstrate that the second scenario reproduces both the observed $d^2N/(dW_r dz)$ and bias data well. We obtain a best-fit transitional mass scale of $\sim 10^{11.5} h^{-1} M_\odot$ and a cold gas fraction (as represented by the Mg^+ ions) of $< 10\%$ in massive halos.

Given the agreement between observations and our halo occupation model, we argue that it is not necessary to invoke additional, complicated star formation feedback for explaining the inverse correlation between W_r and $\langle M \rangle$. We demonstrate that the halo occupation approach allows us to gain physical insights for (1) understanding the origin of intervening absorbers observed in the spectra of background QSOs, and (2) constraining the distribution of baryons in dark matter halos. We discuss these results in the context of gas accretion in recent theoretical developments (i.e., Birnboim & Dekel 2003; Dekel & Birnboim 2006; Kereš et al. 2005; Birnboim et al. 2007).

This paper is organized as the following. In § 2, we outline the theoretical framework for constructing the conditional probability distribution of equivalent widths $P(W_r|M)$. In § 3, we derive the observables that characterize the statistical properties of Mg II absorbers, based on known dark matter halo statistics and $P(W_r|M)$. In § 4, we compare the model predictions with empirical measurements for Mg II absorbers. In § 5, we apply the best-fit model to predict additional statistical quantities on the galaxy-absorber correlation that can be tested with future observations. Finally, we discuss in § 6 the interpretations of our analysis. We adopt a flat Λ CDM cosmology with $\Omega_M = 0.25$ and $\sigma_8 = 0.8$ and a dimensionless Hubble constant $h = H_0/(100 \text{ km s}^{-1} \text{ Mpc}^{-1})$ throughout the paper.

2. THEORETICAL FRAMEWORK

In this section, we describe the approach to populate dark matter halos with cold baryons that are represented by the presence of Mg^+ ions. An implicit assumption of our halo occupation approach is that all absorbers originate in halos, rather than in metal enriched intergalactic medium (IGM) outside of individual halos. This assumption is justified by the strong correlation between absorbers and galaxies; the LRG–Mg II cross-correlation function exhibits a strong signal at separations less than halo radii (Bouché et al. 2004). In addition, for each absorber a galaxy is nearly always found at a separation significantly less than the typical halo radius expected given the galaxy luminosity. Finally, the multi-component nature of Mg II systems demonstrates that the absorbing medium is highly clumped, in contrast to the smoother gas in the IGM.

For each dark matter halo, we will specify two quantities: (1) the mean absorption strength per unit surface mass density $A_W(M)$, and (2) the mean covering factor $\kappa_g(M)$ of the gaseous clouds. These parameters determine the conditional probability distribution of W_r as a function of halo mass, $P(W_r|M)$ which, when combined with known statistics of dark matter halos, allows us to derive theoretical predictions of various statistical properties of Mg II absorbers for direct comparisons with observations.

2.1. Constructing the Gaseous Halo

A dark matter halo is defined as a collapsed and virialized object with a mean interior density equal to 200 times the background density. Thus the radius of a halo is

$$R_h = R_{200} = \left[\frac{3M}{4\pi(200\bar{\rho}_m)} \right]^{1/3}. \quad (1)$$

The choice of $200\bar{\rho}_m$ is motivated by estimates of the virial radius from the spherical collapse model, which predict a value of ~ 180 . While these estimates are idealized, they also match the halos identified in N-body simulations, from which the global properties of halos are calibrated. According to Equation (1), a $10^{12} h^{-1} M_\odot$ halo has a co-moving radius of $243 h^{-1} \text{kpc}$, while R_{200} for a $10^{14} h^{-1} M_\odot$ halo is $1.1 h^{-1} \text{Mpc}$. With this definition, all halos of mass M have the same co-moving radius at any redshift. We adopt the halo mass profile of Navarro et al. (1997) and the concentration-mass relation of Bullock et al. (2001) (with updated parameters from Wechsler et al. 2006) to calculate the halo mass as a function of radius.

We begin with the empirical result that the equivalent width W_r of an absorption system is proportional to the number of absorption components, which we interpret as gas clouds or clumps encountered along the sightline through the halo¹. We adopt an isothermal profile with a core radius a_h to approximate the mean gas density that follows

$$\rho_g(r) = f_g \mathcal{G}_0 (r^2 + a_h^2)^{-1}, \quad (2)$$

where f_g is the gas fraction,

$$\mathcal{G}_0 = \frac{M(< R_g)/4\pi}{R_g - a_h \tan^{-1}(R_g/a_h)}, \quad (3)$$

and $M(< R_g)$ is the mass of dark matter within the effective radius R_g of the gaseous halo. Beyond R_g , no absorption is

¹ We note that an absorption line of width W_r implies a maximum velocity difference between components of $\sim 100 \text{ km s}^{-1}$ per Angstrom. The maximum circular velocity of a $10^{12} h^{-1} M_\odot$ NFW halo is $\sim 150 \text{ km s}^{-1}$.

found. We note that an isothermal distribution of discrete gas clumps is expected to have a mean absorption strength that declines with radius. At a certain impact parameter the mean number of clouds per line of sight will rapidly decline and become negligible (see, e.g., Figure 1 in Chelouche et al. 2007). We approximate this effect by creating an effective gas radius, R_g , beyond which no gas clumps are present.

Considering the total absorption equivalent width W_r as a sum over all clumps encountered along a sightline leads to

$$W_r(s|M) = W_0 \times \left[\frac{2\sigma_{\text{cl}}}{M_{\text{cl}}} \int_0^{\sqrt{R_g^2 - s^2}} \rho_g(\sqrt{s^2 + l^2}) dl \right] \quad (4)$$

$$= \left(\frac{W_0 \sigma_{\text{cl}} f_g}{M_{\text{cl}}} \right) \frac{2\mathcal{G}_0}{\sqrt{s^2 + a_h^2}} \tan^{-1} \sqrt{\frac{R_g^2 - s^2}{s^2 + a_h^2}}, \quad (5)$$

where s is the impact parameter of the sightline with respect to the center of the halo, σ_{cl} and M_{cl} are the cross section and mean mass of individual gas clumps, and W_0 is the absorption per clump. It is clear that the parameters that control the relation between impact parameter and W_r , such as the gas fraction f_g , and the mean absorption strength W_0 and cross-section σ_{cl} of individual clumps, are degenerate. We express their product as a single free parameter

$$A_W \equiv \frac{W_0 \sigma_{\text{cl}} f_g}{M_{\text{cl}}}, \quad (6)$$

which represents the mean absorption equivalent width per unit surface mass density of the cold gas. In the limit that all the components of the absorption line are optically thin, A_W would be a measure of the mean particle density of Mg^+ ions. Some fraction of the lines will be optically thick, however, so we are unable to constrain the density from the values of A_W . The relation between the predicted absorption equivalent width W_r at impact parameter s of a given halo is described by

$$W_r(s|M) = A_W(M) \frac{2\mathcal{G}_0}{\sqrt{s^2 + a_h^2}} \tan^{-1} \sqrt{\frac{R_g^2 - s^2}{s^2 + a_h^2}}. \quad (7)$$

Equation (7) shows that if the fraction of cold gas and its properties do not change across all halo masses, then A_W is expected to be a constant and the total mean equivalent width is expected to increase with halo mass due to the larger gas mass in more massive halos.

We choose a value of $a_h = 0.2R_g$, noting that our results are insensitive to the exact choice for this parameter. We set $R_g = 80$ comoving $h^{-1} \text{kpc}$ ($50 h^{-1} \text{kpc}$ physical at $z = 0.6$) for halos of mass $10^{12} h^{-1} M_\odot$. The gas radius scales as $R_g = 80(M/10^{12})^{1/3} h^{-1} \text{kpc}$, the same scaling as the halo radius in equation (1). With this normalization, the gas radius is roughly one third of the halo radius for all halo masses. The choice of $50 h^{-1} \text{kpc}$ for our fiducial radius is motivated by observations of the radial extent to which Mg II absorption of $W_r \geq 0.3 \text{ \AA}$ is detected around L_* galaxies (e.g., Steidel 1993). We will demonstrate in § 5 that the value of R_g makes distinct predictions for the distribution of impact parameters, and that our choice for R_g matches available observations well.

2.2. The Conditional Probability Distribution of W_r —A Smooth Gaseous Halo Model

To construct the conditional probability distribution of W_r , $P(W_r|M)$, we consider the probability distribution of a random

line of sight intercepting a halo at impact parameter s and the mean absorption expected at the impact parameter s . For a random line of sight, the probability that a sightline passes through a halo of mass M with impact parameter s is

$$P(s|M) = \begin{cases} 2s/R_g^2 & \text{if } s \leq R_g \\ 0 & \text{if } s > R_g. \end{cases} \quad (8)$$

The distribution of W_r is related to the distribution of impact parameters according to

$$P(W_r|M)dW_r = \kappa_g(M)P(s|M)ds, \quad (9)$$

where κ_g is the total probability of detecting an absorber in a halo of mass M , which may be less than unity. This integrated probability that a sight line through a halo yields an absorber is governed by two physical quantities: the mean covering fraction of cold gas per halo and the fraction of halos that host cold gas clouds. These two quantities are degenerate, and we parameterize their product with the quantity κ_g .

From equations (8) and (9), the probability distribution function of equivalent widths is

$$P(W_r|M) = \kappa_g(M) \frac{2s(W_r|M)}{R_g^2} \frac{ds}{dW_r}, \quad (10)$$

where $s(W_r|M)$ is the inversion of equation (7), which is performed numerically. The derivative of s with respect to W_r is

$$\frac{ds}{dW_r} = (2A_W \mathcal{G}_0)^{-1} \left[\frac{s \times \tan^{-1} x}{(s^2 + a_h^2)^{3/2}} + \frac{1 + x^2}{\sqrt{s^2 + a_h^2}} \frac{(a_h^2 + R_g^2)(s \times x)}{(R_g^2 - s^2)(a_h^2 + s^2)} \right]^{-1}, \quad (11)$$

where $x \equiv \sqrt{(R_g^2 - s^2)/(a_h^2 + s^2)}$.

Instead of parameterizing the mass dependence of κ_g using power-laws or polynomials, we adopt a non-parametric approach and specify the values of κ_g at four different masses and spline interpolate between them. Thus, the form of κ_g is fully non-parametric. The four mass values, M_1 through M_4 are $\log M_i = 10.0, 11.33, 12.66, \text{ and } 14.0$. We denote the four parameters of the κ_g function as $\kappa_1, \kappa_2, \kappa_3, \text{ and } \kappa_4$. We perform the interpolation in $\log M$ and $\log \kappa_g$ and extrapolate to higher and lower masses.

In this smooth gaseous halo model, which we will refer to as the ‘‘classical’’ model, we adopt a double power law to account for the mass dependence of the mean absorption per unit surface mass density A_W , i.e.,

$$A_W(M) = \begin{cases} A_0 M_{12}^\alpha & \text{if } M_{12} \leq 1 \\ A_0 M_{12}^\beta & \text{if } M_{12} > 1. \end{cases} \quad (12)$$

As a result, this classical model contains seven free parameters to be constrained by the data. Three govern the amount of absorption as a function of halo mass, A_0, α, β , and four characterize the mass dependence of gas covering fraction κ_1 - κ_4 .

In summary, the gas density profile determines the relative absorption between different impact parameters in a halo—the density profile sets the *shape* of $P(W_r|M)$. The relative absorption between halos of different masses is determined by A_W ; at $s = 0$, the line of sight directly through the center of a halo, the absorption scales as $W_r(0|M) \simeq M_{12}^{1/3} (A_W/10.9)$ where A_W is in units of $(h \text{ \AA cm}^2/\text{gm})$. The incidence of the absorption is set by κ_g . Some sightlines that pass through a halo will encounter no absorbing gas, either due to the fact that the absorbing gas is highly clumpy and the covering fraction is low or due to the fact that the halo does not contain cold gas.

2.3. Incorporating a Cold-Mode/Hot-Mode Transition

As we summarized in § 1, the Mg II absorbers are known to originate in primarily cool, photo-ionized gas. Recent numerical simulations show that stable shocks develop as gas accretes onto a dark matter halo, and above a critical mass threshold all gas is shock heated to the virial temperature or above. At low mass scales, however, gas accreted onto halos is not shock heated, but remains cold as it sinks to the center of the halo (e.g., Kereš et al. 2005). Dekel & Birnboim (2006) demonstrate that this is due to the gas cooling time being too short with respect to the compression time in low mass halos, thus shocks are not stable at any radius within the halo.

It is therefore expected that halos above a certain mass scale may not contribute significantly to the observed Mg II absorbers due to shock heating of their gas. In this second scenario, we include a transitional mass scale, above which the gas becomes predominantly shock-heated and unable to contribute to Mg II absorption. We denote the shock radius R_{sh} . The absorption efficiency at $r < R_{\text{sh}}$ is reduced to a fraction f_{cold} , which represents the fraction of gas that is cold within the shock radius relative to gas outside the shock. For impact parameters smaller than the shock radius, equation (7) is modified as the following,

$$W_r(s|M) = W_r(s|M)_{(R_{\text{sh}}=0)} - (1 - f_{\text{cold}}) A_W \frac{2\mathcal{G}_0}{\sqrt{s^2 + a_h^2}} \tan^{-1} \sqrt{\frac{R_{\text{sh}}^2 - s^2}{s^2 + a_h^2}}, \quad (13)$$

where the first term on the left hand side is the result from equation (7), in which $R_{\text{sh}} = 0$. Equation (11) is calculated for $s < R_{\text{sh}}$ in the same manner.

Figure 1 shows $P(W_r)$ (normalized to $\kappa_g = 1$) for halos of $10^{11.5} h^{-1} M_\odot$ (left panel) and $10^{13} h^{-1} M_\odot$ (right panel). The value of A_W is set such that a sightline at an impact parameter of $R_g/2$ through a $10^{12} h^{-1} M_\odot$ halo yields an equivalent width of 1.5 \AA for comparison purpose. In each panel, we present three different probability distribution functions (PDFs). The dotted curve shows equation (10), which represents the W_r distribution for a continuous gas density profile with no shock. As the impact parameter approaches the edge of the halo, W_r becomes small. It is more likely to go through at halo at large impact parameters, but the projected density drops steeply as s approached R_g , thus $P(W_r) = 0$ at $W_r = 0$. The mode of the distribution occurs at $s \sim 0.9R_g$, and at larger W_r the curve follows W_r^{-3} . The distribution reaches a maximum value of $W_r \sim 3.6 \text{ \AA}$ at $s = 0$.

The dashed curve shows the distribution of equivalent widths for a halo with $R_{\text{sh}} = 0.3R_g$, and $f_{\text{cold}} = 5\%$. The primary effect of shock heated gas in the inner sphere is to reduce the maximum W_r . In the case of a $10^{11.5} h^{-1} M_\odot$ halo, the largest equivalent width is reduced by a factor of two. For $s < R_{\text{sh}}$, $P(W_r)$ has a very different form. As s falls just inside the shock radius, W decreases rapidly. At $s \sim R_{\text{sh}}/2$, $W_r(s)$ reaches a minimum value as the small fraction of cold gas within R_{sh} accumulates enough to contribute to the total absorption. The minimum value of W_r depends on f_{cold} , but around the minimum, the derivative dW_r/ds becomes small, producing a sharp feature in the total $P(W_r)$ curve at $W_r \sim 1 \text{ \AA}$. This feature is even more pronounced in the PDF for the higher mass halo (right panel), also with $R_{\text{sh}} = 0.3R_g$.

The sharp feature is due to the idealized nature of the calculation. In practice, the propagation of the shocks is unlikely to be spherically symmetric, and a halo of Poisson-distributed

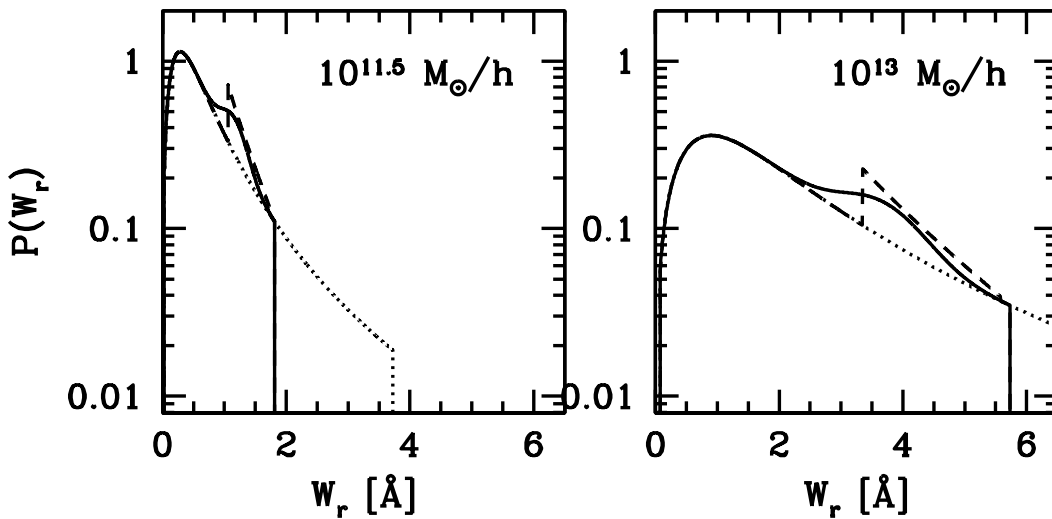


FIG. 1.— The distribution of equivalent widths $P(W_r|M)$ for halos of $10^{11.5} h^{-1} M_\odot$ (left panel) and $10^{13} h^{-1} M_\odot$ (right panel). In both panels, the dotted curve is $P(W_r|M)$ for a model in which the cold gas follows an isothermal density profile throughout the halo. The dashed curves represent a model in which the cold gas within $R = 0.3R_g$ is reduced by a factor of $1 - f_{\text{cold}} = 0.95$. The sharp feature in the PDF is due to slow change in W_r as s approaches 0. The solid curve represents a model where this feature is smoothed out, as expressed in equation (14).

clouds will also smear out this feature. To facilitate the calculations, however, we approximate the distribution of $W_r(s < R_{\text{sh}})$ as a Gaussian centered on $\mu_W = W_r(s = R_{\text{sh}}/2)$ with width $\sigma_W = [W_r(R_{\text{sh}})/2 - W_r(0)]/2$. The amplitude of the Gaussian function is set by the fraction of the cross section within the shock radius, which for $R_{\text{sh}} = 0.3R_g$ is 9%. The Gaussian function is then added to the PDF for $s > R_{\text{sh}}$. For this shocked halo model, the probability distribution is

$$P(W_r|M) = \kappa_g(1 - f_\sigma) \frac{s(W_r|M)}{R_g^2} \frac{ds}{dW_r} + \frac{\kappa_g f_\sigma}{\sqrt{2\pi\sigma_W^2}} \exp\left[-\frac{(W_r - \mu_W)^2}{2\sigma_W^2}\right], \quad W_r \leq W_{\text{max}}, \quad (14)$$

where $f_\sigma = R_{\text{sh}}^2/R_g^2$ is the probability that a sight line has an impact parameter within R_{sh} , and $W_{\text{max}} = \max[W_r(R_{\text{sh}}), W_r(0)]$ from equation (4). We note that $P(W_r) = 0$ for $W_r > W_{\text{max}}$. The results are shown in the solid lines in both panels of Figure 1. Instead of a sharp peak in $P(W_r)$, the smooth model creates a ‘shoulder’ in the PDF, smoothing out the discontinuity in the dashed curve. The parameters of the Gaussian are chosen such that this shoulder tracks the peak in the PDF as R_{sh} changes.

In the one-dimensional simulations of Birnboim & Dekel (2003) and Dekel & Birnboim (2007), shock heating first become stable at the inner regions of the halo, then propagates outward as the halo evolves and becomes more massive. Thus at a given epoch, the width of the transition region in their simulations is roughly a factor of 2–5 in halo mass. In more realistic three-dimensional simulations, but in which the shock fronts are not fully resolved, the fraction of cold gas decreases linearly with $\log M$ over ~ 1 dex in mass (Kereš et al. 2005; Birnboim et al. 2007). We parameterize the mass dependence of R_{sh} as

$$\frac{R_{\text{sh}}}{R_g} = \hat{R}_{\text{sh}}^0 + \gamma_{\text{sh}} \log_{10} M_{12}, \quad (15)$$

and restrict R_{sh}/R_g to be no smaller than 0 and no larger than 1. We will refer to the ‘‘transition scale’’ as the mass at which $R_{\text{sh}}/R_g = 0.5$. At low masses the shock radius is zero, while in the transition region the fraction of the gas radius that is within the shocked core increases linearly with $\log M$ until $R_{\text{sh}} = R_g$. For halos with $R_{\text{sh}} = R_g$, the equivalent width is calculated as

$$W_r(s|M) = f_{\text{cold}} A_W \frac{2\mathcal{G}_0}{\sqrt{s^2 + a_h^2}} \tan^{-1} \sqrt{\frac{R_g^2 - s^2}{s^2 + a_h^2}}. \quad (16)$$

Nominally, this ‘‘transition’’ model has eight free parameters: A_W , κ_1 through κ_4 , \hat{R}_{sh}^0 , γ_{sh} , and f_{cold} . In this scenario, we leave A_W to be invariant with halo mass and attribute relevant mass-dependent gas fraction to R_{sh} and f_{cold} , in order to simplify the model analysis. Removing freedom from A_W in favor of R_{sh} is beneficial in that it highlights the differences between the two scenarios and allows us to isolate features from each model. As we will show in § 4, the classical model and the transition model have distinct predictions for various statistical quantities of the Mg II absorbers. These distinctions can be attributed to the different spatial distributions of the cold gas in halos of different mass, and serve as strong constraints of the models.

3. DERIVATION OF THE OBSERVED STATISTICAL PROPERTIES OF MG II ABSORBERS

Both the frequency distribution of Mg II absorbers as a function of W_r and their clustering amplitude with respect to LRG are known from previous work. Here we summarize these known statistical properties from observations and derive theoretical formulae based on the two scenarios described in § 2.

3.1. The Frequency Distribution Function

The frequency distribution function is defined as the number of absorbers per absorption equivalent width interval

per unit redshift path length. Here we combine the results from Prochter et al. (2006) for $W_r > 1 \text{ \AA}$ with the results from Steidel & Sargent (1992) for $0.3 \text{ \AA} \leq W_r \leq 1 \text{ \AA}$. The Prochter et al. (2006) data is nearly complete ($> 95\%$) over the redshift range $0.4 \leq z \leq 2.2$ for absorbers of $W_r > 1 \text{ \AA}$. The Steidel & Sargent (1992) data is complete to $W_r = 0.3 \text{ \AA}$ over the redshift range $0.2 \leq z \leq 2.2$.

For empirical measurements, we take the raw number counts from Prochter et al. (2006) and divide the number counts by the total co-moving path length of all the lines of sight, l_{tot} . The total co-moving path length is calculated by integrating the distance-redshift relation, weighted by the number of lines of sight $g(z)$ at each redshift interval dz as follows,

$$l_{\text{tot}} = \int dz g(z) [\Omega_m(1+z)^3 + \Omega_\Lambda]^{-1/2}. \quad (17)$$

Equation (17) yields the total co-moving radial distance covered by the lines of sight to $\sim 45,000$ quasars available in SDSS DR3. The total number of absorbers is $N_{\text{abs}} = 4835$, with $l_{\text{tot}} = 4.55 \times 10^7 h^{-1} \text{ Mpc}$. There is no systematic or cosmic variance error estimate for the frequency data, so we apply Poisson fluctuations for estimating random errors, including a 5% ‘systematic’ uncertainty for each of the 38 bins that have at least one absorber. This additional systematic error only alters the total uncertainty for the lowest few W_r bins from the Prochter et al. sample ($W_r = 1 - 1.5 \text{ \AA}$) and prevents those data from driving the total χ^2 when evaluating a model. For $W_r \leq 1 \text{ \AA}$, we use the results from Steidel & Sargent (1992). This is a much smaller sample, but is valuable for constraining the shape of $d^2N/(dW dl)$. The Steidel & Sargent measurements are scaled to those of the Prochter et al. (2006) data for $1 \text{ \AA} < W_r \leq 1.3 \text{ \AA}$ to account for the difference in the total redshift survey paths of the two samples.

To obtain theoretical predictions, we calculate the conditional probability of a halo containing an absorber of a given strength $P(W_r|M)$ as specified in § 2 for a given set of parameters. The integral of the product of the cross-section weighted halo mass function and the probability of detecting an absorber of W_r in a halo of a given mass leads to the frequency of the absorbers versus W_r , i.e.

$$f(W_r) \equiv \frac{d^2N}{dW_r dl} = \int dM \frac{dn}{dM} \sigma_g(M) P(W_r|M), \quad (18)$$

where $\sigma_g(M) = \pi R_g^2$ is the cross section of the gas halo and dn/dM is the halo mass function. The frequency distribution in equation (18) has units of $\text{\AA}^{-1} (h^{-1} \text{ Mpc})^{-1}$ in co-moving coordinates.

We note that two scaling factors need to be accounted for before a direct comparison between empirical measurements and model predictions can be done. First, the redshift distributions of the frequency data and the bias data are different. As discussed in § 3.2 below, the bias data are limited by the redshift range for LRGs at $0.35 < z < 0.8$. We therefore must re-normalize the frequency function to the effective redshift of the B06 sample at $z = 0.6$. The amplitude of the frequency function rises between $z = 0.5$ and $z = 1$, and the ratio of dN/dz at $z = 0.6$ to the full sample is 0.55. Second, the amplitude of $f(W_r)$ based on a SDSS DR5 Mg II absorber sample is found to increase by a factor of 1.1 (J. X. Prochaska, private communication). We have therefore included this correction in

our empirical data for comparisons with models².

3.2. The Mg II–LRG Cross-Correlation Function

The cross-correlation function between absorbers and galaxies along common lines of sight determines the clustering strength (and therefore the relative bias) of the absorbers with respect to the galaxies. Given the mean mass scale of the halos that host the galaxies, one can derive the mean mass scale of the halos hosting the absorbers. Bouché et al. (2006) presented the projected cross-correlation function of Mg II absorbers and LRGs on scales of $r_p = 1 - 10 h^{-1} \text{ Mpc}$. The Mg II–LRG sample covers a redshift range of $0.35 < z < 0.8$. These authors calculate the relative bias of absorbers to LRGs by taking the ratio of absorber–LRG cross-correlation function to the LRG autocorrelation function,

$$\hat{b}_W \equiv \frac{b_W}{b_G} = \frac{\xi_{WG}}{\xi_{GG}}. \quad (19)$$

Equation (19) is only exact at large scales because it assumes linear bias, but the scale dependence of halo bias is largely independent of halo mass (Tinker et al. 2005) and will cancel in the ratio. We take the absolute bias of LRGs with respect to dark matter to be $b_{\text{LRG}} = 1.85$ at $z = 0.6$ (White et al. 2007, who adopt the same cosmology as what is assumed here), and estimate the absolute bias of the absorbers following Equation (19).

To compare the models to the data, we calculate the absolute bias of absorbers and divide the calculation by b_{LRG} . The bias data are in four bins of W_r : $[0.3, 1.15] \text{ \AA}$, $[1.15, 2.0] \text{ \AA}$, $[2.0, 2.85] \text{ \AA}$, and $[2.85, 4.0] \text{ \AA}$. The highest- W_r bin has little influence on the parameter constraints due to the small number of objects in that bin. When comparing models to bias data, we take the number-weighted average bias over the given range in W_r . The B06 sample is incomplete for $W_r < 1 \text{ \AA}$. The true frequency distribution monotonically increases with smaller W_r , but the $[0.3, 1.15] \text{ \AA}$ bin is dominated by $\sim 1 \text{ \AA}$ absorbers. When calculating \hat{b}_W in this bin, we introduce the same incompleteness in the model by multiplying $P(W_r|M)$ by $21.4(1 - W_r)$ for $W_r < 1 \text{ \AA}$. With this factor, a model that accurately re-produces the true $d^2N/(dW_r dl)$ data will produce a frequency distribution that matches the shape of the B06 sample.

In the context of the halo model, the bias of absorbers with respect to the dark matter is equal to the mean halo bias, weighted by the probability of finding an absorber W_r at mass M ;

$$b_W = \frac{1}{f(W_r)} \int dM \frac{dn}{dM} \sigma_g(M) b_h(M) P(W_r|M), \quad (20)$$

where b_h is the halo bias. For the halo mass function we use the fitting function of Warren et al. (2006), while for the halo bias we use the fitting function of Tinker et al. (2005). All halo properties are calculated at the effective redshift of the B06 absorber sample. The redshift range of the data is large enough such that integrating equations (18) and (20) over redshift will yield slightly different results, but for the purpose of this study it is sufficient to choose an effective redshift for all

² We note that the slope of the full Prochter et al. (2006) sample is $d \log N / dW = 0.72$, a value consistent with the results from Nestor et al. (2005), who calculate $d \log N / dW = 0.75$ over $0.4 < z < 0.8$ for a smaller sample culled from the SDSS early data release.

calculations. In our subsequent analyses, the redshift evolution of $f(W_r)$ will be used as an additional constraint on the models.

4. COMPARISONS BETWEEN OBSERVATIONS AND BEST-FIT MODELS

The scenarios discussed in § 2 have distinct predictions for the empirical data discussed in § 3. We constrain the models using a Monte Carlo Markov Chain technique that determines the best-fit parameters based on comparisons of the data with random realizations from various model predictions. For each realization in the chain, the total χ^2 is the sum of the χ^2 values from both the frequency and bias data. We will refer to these quantities as χ_f^2 and χ_b^2 , respectively. Because of the larger number of frequency data and smaller errors on those data, χ_f^2 dominates the total χ^2 . However, the χ_b^2 values should be taken with caution, because we have no true estimate of the cosmic variance.

4.1. The Classical Gaseous Halo Model

As described in § 2.2, the classical model contains seven free parameters, including three that characterize the absorbing gas column, A_W , for halos of different mass scales and four that characterize gas covering fraction κ_1 - κ_4 of individual halos. The mass dependence in A_W allows the predicted W_r versus impact parameter s relation (Equation 7) to vary smoothly with halo mass. The best-fit parameters are listed in Table 1. Figure 2 compares observational data with predictions based on the “classical” model (dotted curves).

We present in panel (a) the frequency data and in panel (b) the residuals normalized by the corresponding error of each bin. The frequency data are adequately fit by this model, yielding $\chi_f^2 = 43.3$ for 41 data points and seven free parameters. The classical model matches the abundance of strong absorbers, $W_r > 2 \text{ \AA}$, but at lower equivalent widths the residuals become large. Specifically, this model overproduces the number of absorbers by nearly 60% at $W \sim 0.3 \text{ \AA}$ due to a large contribution from low-mass halos.

We present the comparison for the halo bias of the absorbers in panel (c) and the inferred mean halo mass in panel (d). The bias data (points with errorbars) are derived from Mg II-LRG cross-correlation measurements. The relative bias \hat{b}_W derived from observations decreases from 0.8 at $\langle W_r \rangle \approx 0.8 \text{ \AA}$ to nearly 0.4 at $\langle W_r \rangle \approx 2.4 \text{ \AA}$. The measured bias for $W_r \geq 2.8 \text{ \AA}$ increases slightly to 0.5, but the number of objects in this bin is small and it has little influence on our fitting results. Using a simple mean-mass approximation, B06 infer a decrease in mean halo mass of nearly 1.5 dex over this range in W_r . The best-fit classical model is unable to reproduce the inverse correlation between \hat{b}_W and W_r . As expected, the bias monotonically increases with W_r , placing the weakest absorbers in $M = 10^{11.5} h^{-1} M_\odot$ halos while locating the strongest absorbers in the nearly same halos as LRGs.

Figures 3a-3b present the parameter constraints for this model. In both panels, the inner and outer shaded regions show the allowed parameter range, constrained respectively by $\Delta\chi^2 < 1$ and < 4 from the best-fit model. Figure 3a presents the constraints on the mean gas covering fraction κ_g as a function of halo mass. The function peaks at $\log M \approx 12$; nearly all halos of $\log M \approx 11.5 - 12.5$ are expected to produce an absorber if the impact parameter is less than R_g to a background quasar. At lower and higher masses, κ_g rapidly falls off, but the constraints become weak at the extrema of the

mass range. Given the constraints, there is little contribution to Mg II absorption from halos more massive than $10^{13} h^{-1} M_\odot$ and less massive than $3 \times 10^{10} h^{-1} M_\odot$.

Figure 3b shows constraints for the absorption column $A_W(M)$. For low-mass halos, the constraints on the slope and normalization are strong; $10^{12} h^{-1} M_\odot$ halos produce $\sim 1 \text{ \AA}$ absorbers. The best-fit model has a single power-law, with $\alpha \approx \beta \approx -0.17$. The negative values of α and β increase the absorption efficiency in lower mass halos, but not sufficiently to produce an anti-correlation between W_r and M . A slope more negative than $-1/3$ in $A_W(M)$ versus M is required to make the mean W_r constant as a function of M , but these negative values would violate the constraints on the frequency distribution by overproducing high- W_r absorbers.

At $M > 10^{12} h^{-1} M_\odot$, the constraints on A_W are poor because κ_g falls off rapidly at these masses. There is a degeneracy between κ_4 and β ; if κ_g falls off for $M > 10^{12} h^{-1} M_\odot$, high- W_r systems can only be produced if β is large. However, this steepens the slope of \hat{b}_W and these models fare even worse in comparison to the bias data. The models which produce the lowest χ_b^2 have negative values of both α and β .

Figure 3c shows the relative contribution to absorber counts from halos of different mass based on the best-fit model. We refer to this mass distribution as the “occupation function”. The curves show three values of W_r : 0.5 \AA , 1 \AA , and 2 \AA , and the relative areas under the curves represent the relative number of absorbers. The y-axis, in arbitrary units, is the probability of detecting an absorber of W_r in a halo of mass M , i.e., $P(W_r|M)P(M)$, where $P(M)$ is the probability that a given line of sight intersects a halo of mass M based on a cross-section weighted halo mass function, $\sigma_g(M)dn/dM$. These curves have the Gaussian-type shape of the κ_g function, with the sharp edges near the peak resulting from the mass range over which κ_g is truncated at unity. The mass dispersion is ~ 1 dex in $\log M$ for all three curves. The modes of each curve move to higher mass, producing the increasing trend of W_r with M shown in Figure 2d.

In summary, the “classical” model with a smooth gaseous halo *cannot* fit both the frequency data and the bias data simultaneously. Under this scenario, more massive halos are expected to contain more absorbing gas, resulting in a positive correlation between W_r and halo mass M . Forcing the mean absorption A_W per halo to decline steeply with increasing halo mass would improve the model fit to the bias data, but at the same time it would over-produce the abundance of strong ($W_r > 2 \text{ \AA}$) absorbers.

4.2. The Significance of Shock-Heated Gas in Massive Halos

The best-fit parameters of the transition model are also listed in Table 1. This transition model has eight free parameters: A_W , κ_1 through κ_4 , \hat{R}_{sh}^0 , γ_{sh} , and f_{cold} . As discussed in § 2.3, we have left A_W to be invariant with halo mass and attributed relevant mass-dependent gas fraction to R_{sh} and f_{cold} . Comparisons between observations and predictions based on the transition model are also presented in Figure 2 (solid curves).

The addition of the cold-hot transition produces a best-fit model that precisely fits the frequency data over the entire W_r range, including those points at $W < 1 \text{ \AA}$, with $\chi_f^2 = 19.8$. The model also reproduces the anti-correlation between W_r and \hat{b}_W for $W_r < 2.5 \text{ \AA}$, shown in Figure 2c. Although the slope

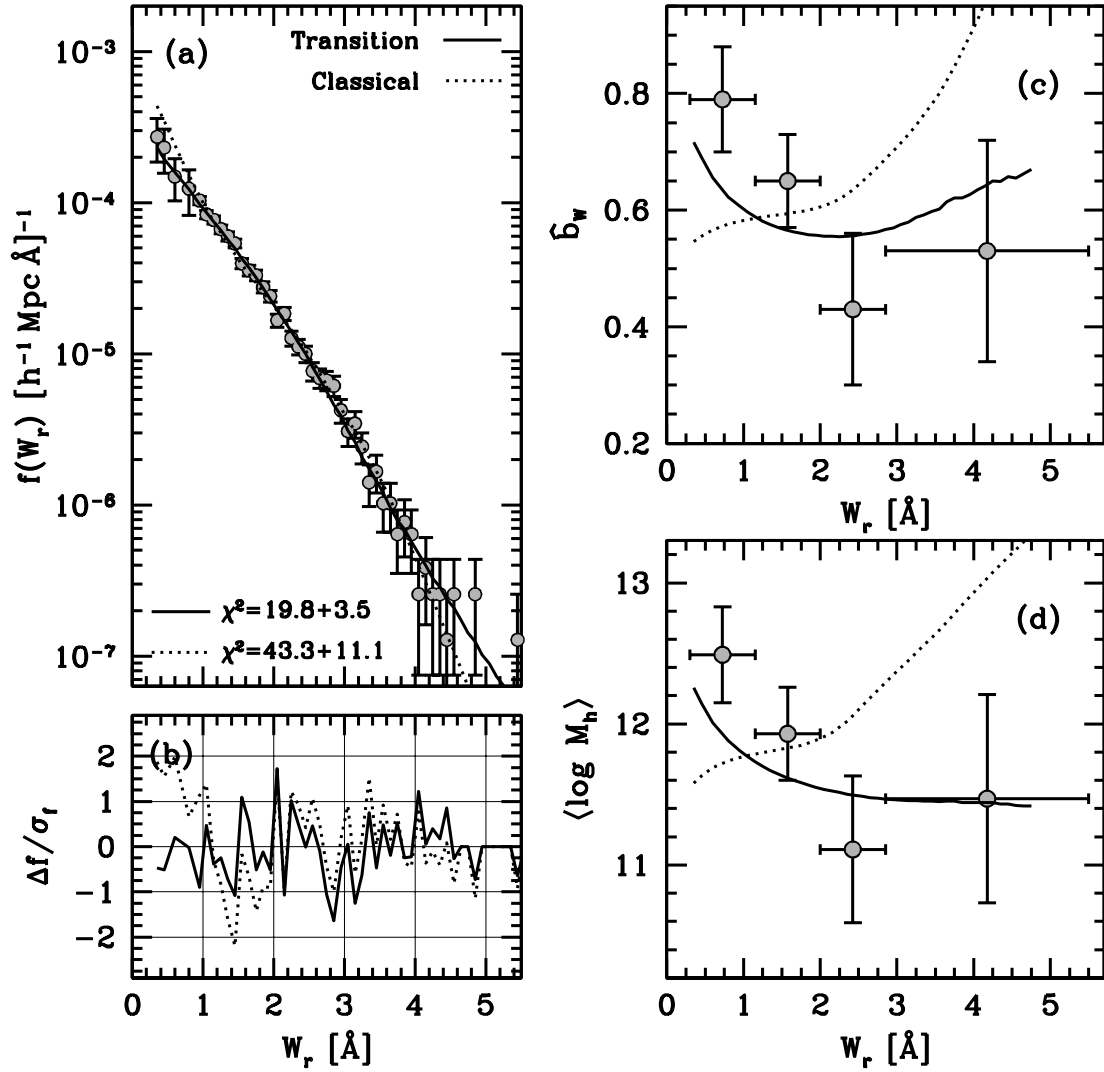


FIG. 2.— Panel (a) The frequency distribution of Mg II absorbers as a function of equivalent width W_r . The points with error bars represent a combination of the data sets of Prochter et al. (2006) ($W_r > 1\text{\AA}$) and Steidel & Sargent (1992) ($W_r < 1\text{\AA}$). The transition between the two data sets is seen easily in the relative error bars between low and high W_r . The solid and dotted curves represent the best-fit models listed in Table 1. The solid curve is the model with a cold-hot transition in halo gas, while the dotted curve has a smoothly varying cold gas fraction as a function of halo mass. The χ^2 values are broken into the χ^2 for the frequency and bias data, respectively. Panel (b): The residuals of the model $f(W_r)$ curves, normalized by the errors on the data. Panel (c): The bias of absorbers relative to LRGs, \hat{b}_W , as a function of W_r . The points with errors are the measurements of Bouché et al. (2006). The solid and dotted curves are the two models from panel (a). Panel (d): The mean logarithmic halo mass as a function of W_r . Points with error bars are the values inferred from the bias data by B06 (not used in the fit). Solid and dotted curves are the two best-fit models.

TABLE 1
PARAMETERS OF THE BEST-FIT MODELS

Model	A_W	\hat{R}_{sh}^0	γ_{sh}	$\log \kappa_1$	$\log \kappa_2$	$\log \kappa_3$	$\log \kappa_4$	α	β	f_{cold}	χ_f^2	χ_b^2
Classical	33.2	—	—	-1.721	-0.012	-0.198	-1.763	-0.172	-0.176	—	43.3	11.1
Transition	136	1.02	1.03	-9.27	-0.205	-0.006	-0.168	—	—	0.061	19.8	3.5

NOTE. — The units of A_W are [$h \text{\AA} \text{cm}^2/\text{gm}$].

of the trend is not as strong as that seen in the B06 measurements, $\chi_b^2 = 3.5$ for four data points. The relative bias in the model decreases from $\hat{b}_W = 0.7$ at $W_r = 0.4\text{\AA}$ to $\hat{b}_W = 0.55$ for

$W_r = 2\text{\AA}$. This declining trend in the absorber bias is due to a decrease in the mean halo mass with increasing W_r (Figure 2d). The mean mass falls by nearly a decade from $W_r = 0.4\text{\AA}$

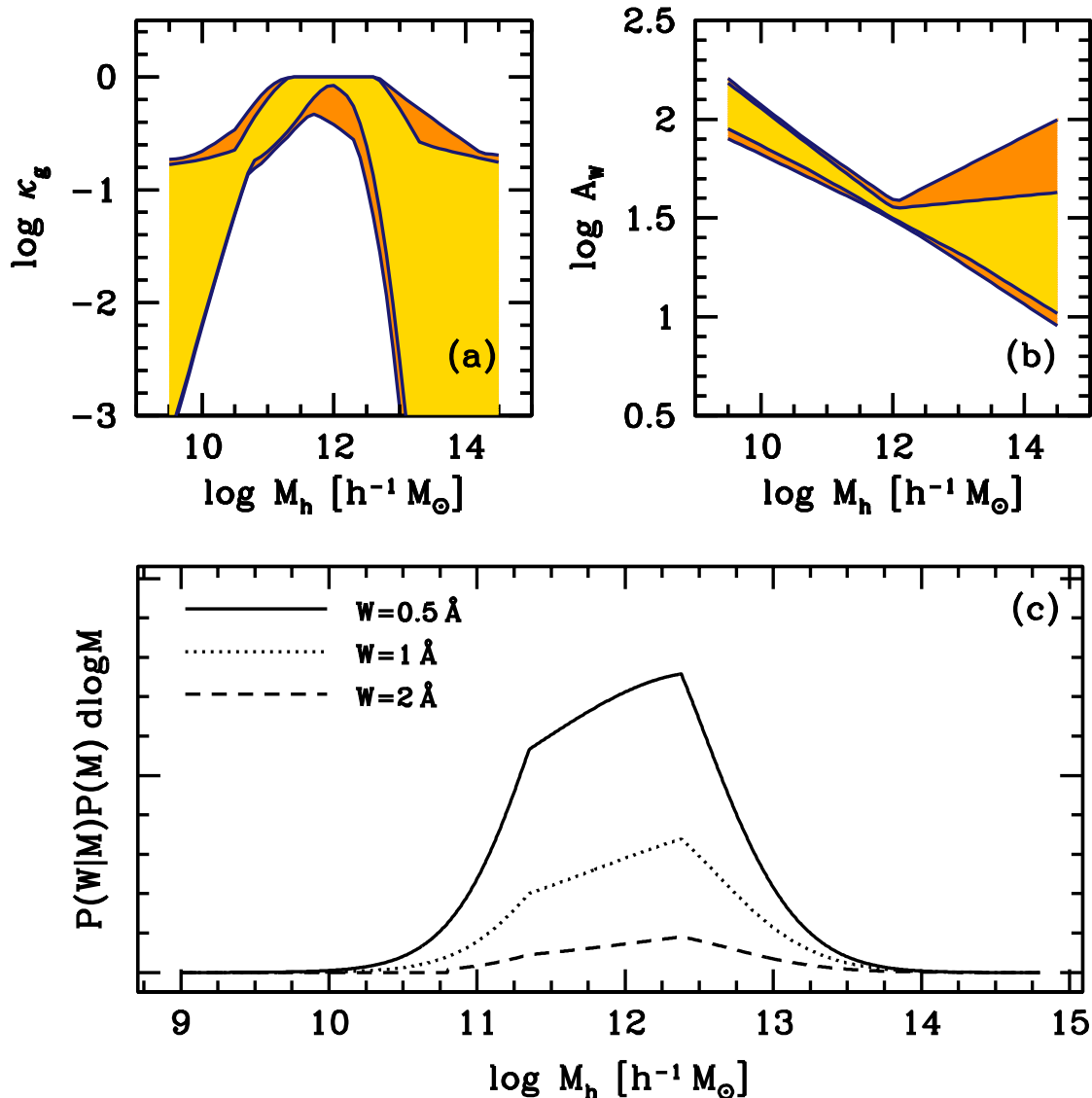


FIG. 3.— Panel (a): Constraints on the covering fraction κ_g as a function of halo mass from the classical model. Inner and outer contours represent the range in models that produce $\Delta\chi^2 < 1$ and 4 with respect to the best-fit model. Panel (b): Constraints on the mean absorption strength per unit gas mass density $A_w(M)$. Contours are for the range of models described in panel (a). Panel (c): The occupation function of absorbers for three different equivalent width values: 0.5 Å, 1 Å, and 2 Å. The y-axis, in arbitrary units, is the probability that a sightline passes through a halo of mass M ($P(M)$) multiplied by the probability that a halo of mass M yields a W_r absorber ($P(W_r|M)$).

to $W_r = 4 \text{ \AA}$.³

The total χ^2 for this model is 23.3 for 37 degrees of freedom. In a purely statistical sense this suggests that the model has too many free parameters. However, we note once again that the errors on $f(W_r)$ are estimates only, and we wish to include as much freedom in the model to prevent the frequency data from driving the constraints on the halo occupation. In this sense, χ_b^2 is the most relevant quantity, noting that eight free parameters is barely sufficient to reproduce the bias measurements.

Figures 4a and 4b present the parameter constraints for the transition model. The covering fraction is narrower and

³ We note that the masses derived by B06 depend on both the model used and the cosmology adopted, and they are not utilized in the fit. Even a perfect fit to the bias data in panel (c) will not necessarily yield the B06 masses in panel (d).

sharper than the classical model: $\kappa_g = 1$ for halos of $\log M \approx 11.5 - 12.5$ and cuts off sharply at lower masses. Over nearly a decade in halo mass, all models with $\Delta\chi^2 < 4$ yield $\kappa_g = 1$. However, the transition from cold mode ($R_{\text{sh}}/R_g = 0$) to hot mode ($R_{\text{sh}}/R_g = 1$) begins at $M \approx 10^{11} h^{-1} M_\odot$ and ends at $M \approx 10^{12} h^{-1} M_\odot$. This indicates that massive halos of $\log M \geq 12$ contribute to the observed Mg II statistics through the presence of cold flow in the shock-heated halos. The constraints on the cold fraction within the shock are strong, with the best-fit model yielding $f_{\text{cold}} = 0.06$ with an allowed range of ± 0.03 for models with $\Delta\chi^2 < 4$. Both the transitional mass scale and cold gas fraction in massive halos agree well with the simulations of Kereš et al. (2005) and Birnboim et al. (2007). In the post-shock regime $\log M > 12.5$, the constraints on the covering factor are poor; models with a low κ_4 yield better fits to the frequency data while high covering factors at

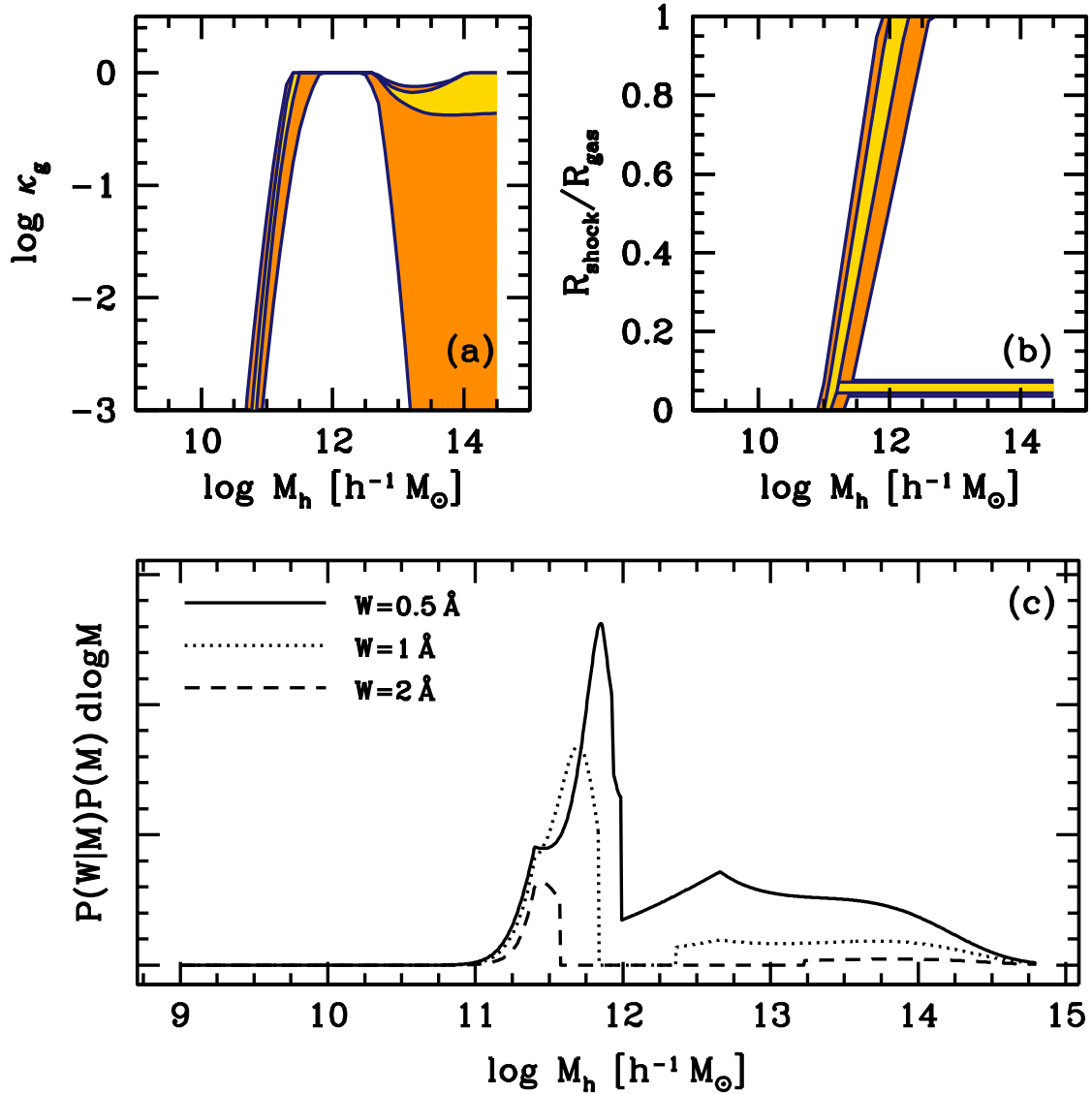


FIG. 4.— Panel (a): Constraints on the covering fraction κ_g as a function of halo mass from the transition model. Inner and outer contours represent the range in models that produce $\Delta\chi^2 < 1$ and 4 with respect to the best-fit model. Panel (b): Constraints on the shock radius R_{sh} (relative to the gas radius). Contours are for the range of models described in panel (a). The horizontal bands to the right of the R_{sh} contours represent the constraints on f_{cold} . Panel (c): The occupation function of absorbers from the best-fit model. The abrupt transition at $M = 10^{12} h^{-1} M_\odot$ is due to R_{sh} becoming larger than R_g .

$10^{14} h^{-1} M_\odot$ produce higher bias factors and lower χ_b^2 .

Figure 4c shows the occupation functions for the best-fit model. For halos of $M = 10^{11} - 10^{12} h^{-1} M_\odot$, the absorber counts rises as κ_g increases with halo mass as shown in panel (a). For $W_r = 0.5 \text{ \AA}$, the occupation function peaks are $10^{12} h^{-1} M_\odot$, then abruptly drops when $R_{\text{sh}} = R_g$ and all halos enter the hot phase. For $W_r = 1$ and 2 \AA , the peak in the occupation functions occur at $10^{11.7} h^{-1} M_\odot$ and $10^{11.5} h^{-1} M_\odot$, respectively. This trend is due to the inside-out nature of the heating; higher- W_r systems are produced at smaller impact parameters and the shock radius envelopes that radius at lower halo masses. Above $10^{12} h^{-1} M_\odot$, the occupation has a tail out to $10^{14} h^{-1} M_\odot$. In the best-fit model, $\kappa_4 = 0.67$, implying that a significant fraction of cluster-sized halos contain some cold gas with a high covering fraction. However, we note again that the constraint on κ_4 is poor due to the low frequency of such massive halos.

For $W_r \geq 1 \text{ \AA}$ absorbers, halos in the post-shock regime do not initially have enough gas to produce absorbers of this strength, and so the distribution of halo masses occupied by these absorbers becomes bimodal; only at $M > 10^{12.5-13} h^{-1} M_\odot$ is there enough cold gas to produce absorbers of this strength. For $W_r = 2 \text{ \AA}$, for example, halos between $10^{11.6}$ and $10^{13.2} h^{-1} M_\odot$ halos do not produce strong absorbers. This bimodal distribution is what causes \hat{b}_W to increase for $W_r > 3 \text{ \AA}$, while $\langle \log M \rangle$ remains constant in Figure 2; bias increases non-linearly with mass, weighting high-mass halos more in \hat{b}_W than in $\langle \log M \rangle$.

In summary, the transition model can simultaneously reproduce the observed frequency data and bias data of Mg II absorbers. The anti-correlation between W_r and M in the transition model is produced through two mechanisms. First, as the shock propagates outward from the center of a massive

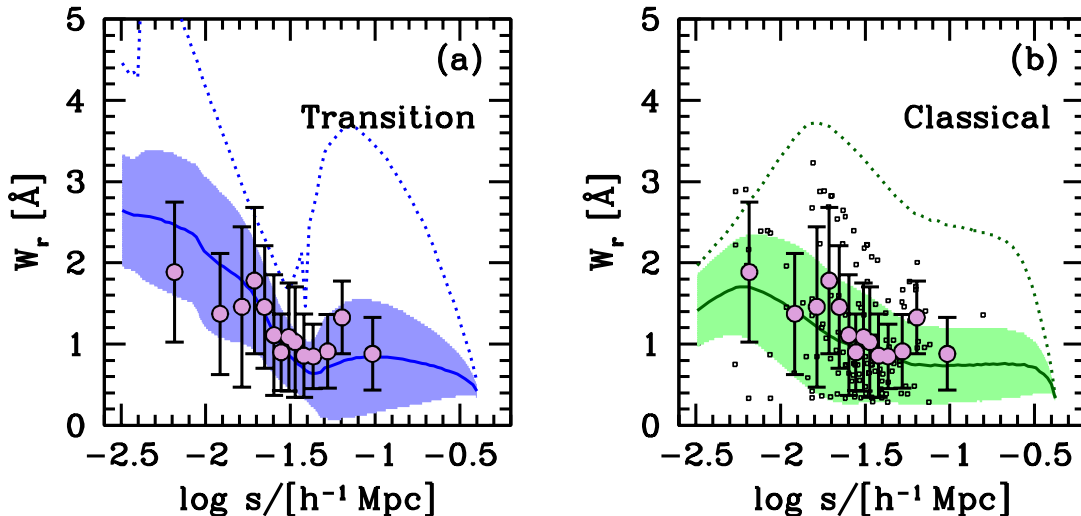


FIG. 5.— The distribution of equivalent width as a function of impact parameter. In both panels, the points represent the mean W_r as a function of $\log s$ from a combination of four sets of data, while the errors show the dispersion about the mean. Panel (a) shows the predictions for the transition model. The solid curve plots the mean W_r while the shaded region represents the predicted dispersion. The dotted curve is the upper-99% bound on the distribution of W_r at each $\log s$. Panel (b) presents the predictions for the classical model. The small open squares represent each individual system in the observational sample. The x -axis is in physical units.

halo, high- W_r systems are no longer produced, but low- W_r systems are produced *more frequently* because sight lines at low impact parameters ($s \leq R_{\text{sh}}$) now produce weaker absorbers. This is demonstrated in Figure 4c by the location of the cutoff in the occupation function—as W_r increases the location of the cutoff moves to lower masses. Second, the small amount of cold gas in the post-shock regime (masses at which $R_{\text{sh}} = R_g$) yields mostly low- W_r absorbers in high mass halos. An instantaneous transition between the cold-mode and hot-mode with a non-zero cold fraction could produce a weak $W_r - M$ anti-correlation. A broad transition region (a small value of γ_{sh}) with $f_{\text{cold}} = 0$ could also produce a weak anti-correlation. In this model the two effects work together to fit the measurements.

5. ADDITIONAL OBSERVABLES PREDICTED BY THE MODELS

We have demonstrated that the transition model can reproduce both the observed frequency distribution function and the Mg II–LRG relative bias data. Given the known $W_r(s|M)$ constrained by the data in § 4, and known mass distribution function of the dark matter halos, we can also predict (1) the correlation between W_r and galaxy impact parameter s , and (2) the impact parameter distribution of Mg II absorbing galaxies $P(s)$. Here we derive these properties on the basis of the gaseous halo model described in § 2 and the best-fit parameters constrained by the frequency and bias data in Table 1.

5.1. The Absorber W_r vs. Galaxy Impact Parameter Correlation

To estimate the correlation between W_r and impact parameter, as well as the distribution of impact parameters, we adopt the center of each halo as the location of the corresponding absorbing galaxy. At a given impact parameter, the distribution of equivalent widths is then determined by

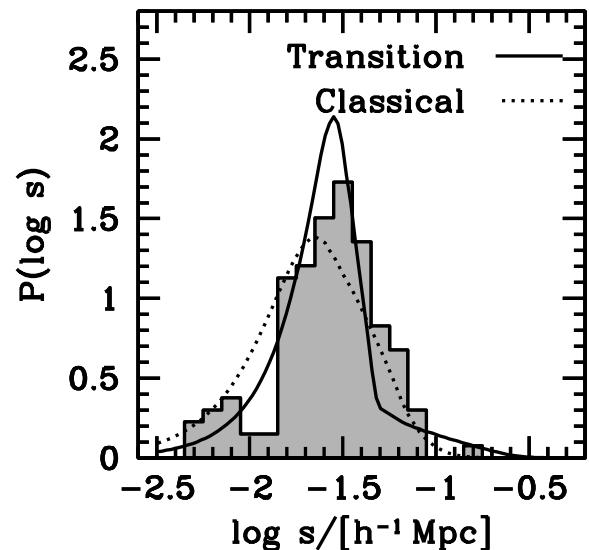


FIG. 6.— The distribution of impact parameters for all absorbers with $W_r > 0.3 \text{ \AA}$. The shaded histogram represents the data presented in Figure 5. The solid and dotted curves show the predictions from the transition and classical models, respectively. The x -axis is in physical units.

$$\begin{aligned}
 P(W_r|s) &= \int dM \frac{dn}{dM} \sigma_g(M) P(W_r|M, s) P(s|M) \\
 &= \int dM \frac{dn}{dM} \sigma_g(M) \delta(W_r(s|M) - W_r) \kappa_g(M) P(s|M)
 \end{aligned} \tag{21}$$

where $P(s|M)$ is the probability distribution of impact parameters of random sightlines defined in equation (8) and $\delta(x)$ is a delta function. From equation (21), the total number of absorbers at a given impact parameter—and thus the distribution of impact parameters as a function of s —is obtained by integrating $P(W_r|s)$ over all W_r .

To use galaxy-absorber pair statistics to constrain the model parameters requires a Mg II absorber survey carried out along the sightlines where the galaxies positions are known *a priori*. Typical absorbing galaxy studies focus on searching for galaxies that give rise to known absorbers. These galaxy-absorber pairs collected from these studies are not suitable for constraining the covering fraction of Mg II gas random halos because sightlines that do not encounter a Mg II absorber are by design excluded from the sample. Therefore, the impact parameter distribution established based on these *absorber oriented* studies is expected to be skewed. A galaxy–Mg II absorber pair sample established in a *galaxy oriented* survey is only mentioned in Tripp & Bowen (2005), but the sample is small and details are not available in the literature.

In the subsequent discussion, we have compiled an *ad hoc* sample of 133 galaxy–Mg II absorber pairs from the literature (Steidel 1995; Kacprzak et al. 2007; Bergeron & Boissé 1991; B06), in which the galaxies are found for known Mg II absorbers. The mean redshift of these samples is $z \sim 0.6$. We note a potential bias in this heterogeneous pair sample. Because of different selection criteria, these pairs are most likely incomplete at impact parameters $s \lesssim 15 h^{-1}$ kpc due to blending of the galaxy light with the QSO. The likelihood of mis-identifying the associated galaxy at $s \gtrsim 60 h^{-1}$ kpc is non-negligible, if the true associated galaxy is too faint to be detected. While we cannot address the covering fraction of Mg II gas in typical galaxies, this pair sample offers a test of our model based on the observed W_r - $\log s$ distribution of known absorbers. This sample also offers an important consistency check on our choice of gas radius.

In Figures 5a and 5b, we compare the predicted W_r - $\log s$ relations from the classical and shocked halo models to observational data. Each point with error bars in Figure 5 is the mean and dispersion from every 10 galaxy-absorber pairs, ordered by $\log s$. It should be noted that the error bars do not represent the error in the mean but rather the variance in W_r at fixed s , which is a physically meaningful quantity that can be compared to models as well. The data show a weak trend of decreasing W_r with larger impact parameter, with $W_r \sim 1.6 \text{ \AA}$ at $-2.3 < \log s < -1.6$ and $W_r \sim 0.9 \text{ \AA}$ at $\log s \gtrsim 1.6$. The dispersion in W_r also decreases from low to high s . There is an “upper envelope” to the data in the W_r - $\log s$ plane such that the highest- W_r systems are preferentially at lower impact parameters (see panel *b*). All distances are in physical units.

In Figure 5a, the predictions for the shocked halo model are shown. The solid curve is the mean equivalent width $\langle W_r \rangle$ as a function of $\log s$. The shaded area is the predicted dispersion in W_r . The size of the dispersion reflects the distribution of halo masses that contribute $W_r > 0.3 \text{ \AA}$ absorbers. The dotted curve is the upper-99% bound on the distribution of $P(W_r|s)$. For $\log s > -1.8$, both the predicted $\langle W_r \rangle$ - $\log s$ mean relation and the associated dispersion in W_r are well rendered in this model. At fixed s , the mean W_r and the dispersion around that value reflect the mean and dispersion in halo mass. A broader distribution of halo masses in κ_g will produce a larger dispersion in W_r at fixed impact parameter. *The decrease in $\langle W_r \rangle$ with $\log s$ results from the fact that in the models the gaseous*

halos are being probed preferentially at their edges at larger s , where the gas density is low. The dispersion decreases because the range in halo masses that can be probed decreases; at large s , smaller halos can no longer be detected and the variance in W_r decreases. The inflection in the model predictions at $\log s \sim -1.5$ occurs at the cold-hot transition scale, and only halos in the hot mode are large enough to produce impact parameters above $50 h^{-1}$ kpc. In the immediate post-shock regime, only very weak absorbers can be produced, so the dispersion in W_r reaches a local minimum at this scale.

For comparison, the predictions from the classical model are shown in Figure 5b. The open squares in this figure show the individual absorbers, elucidating the upper envelope of W_r in the data. At $\log s > -1.8$, the $\langle W_r \rangle$ - $\log s$ trend is similar to the transition model, and the upper-99% bound matches the observational sample. B06 argue that the upper envelope and the trend of $\langle W_r \rangle$ in the data necessitate a M - W_r anticorrelation. The results of the classical model invalidate this argument; stronger absorbers occur at lower s simply because, at fixed halo mass, $W_r(s)$ monotonically increases toward the center of the halo.

5.2. The Impact Parameter Distribution of Mg II Galaxies

Figure 6 shows the distribution of impact parameters for absorbers of all strength, in comparison to model predictions. The gray shaded histogram established from the heterogeneous pair sample exhibits some hint of incompleteness of pairs at $\log s < -1.8$, while the distribution at larger $\log s$ appears relatively well sampled. The distribution of empirical data is roughly Gaussian in $\log s$ with slight negative skewness. This asymmetry may be physical, but could also be due to incompleteness. The solid curve, showing the model prediction, locates the mode at $30 h^{-1}$ kpc, in good agreement with the data. The shape and dispersion are also in good agreement with the data. The distribution predicted by the classical model places the mode at roughly $\sim 20 h^{-1}$ kpc, and the distribution is broader than both the transition model and the data, reflecting the broad shape of the κ_g function in the best-fit classical model.

In a broader sense, the results of Figure 6 support our choice of $R_g \approx R_{200}/3$ for the extent of the Mg II gas. If $R_g = R_{200}$, the modes of each histogram would be shifted by 0.5 dex, making them incompatible with the data. The predictions in Figures 5a and 5b would also be shifted over by the same amount. Setting $R_g = R_{200}$ would have no effect on the accuracy of the fits to the frequency or bias data in Figure 2. Increasing the total gas cross section $\sigma_g(M)$ by a factor of 9 can be compensated for by lowering κ_g by the same factor. But values of κ_g that low would conflict with observational estimates of the covering factor, which vary between 50% and 100% (Steidel et al. 1997; Tripp & Bowen 2005). This demonstrates the potential of a complete sample of absorber-galaxy pairs for constraining models. Finally, we note that a representative sample of Mg II absorbing galaxies will also allow us to derive more quantitative constraints on the luminosity distribution of the absorbing galaxy population.

6. SUMMARY AND DISCUSSION

We have presented a theoretical approach for interpreting the statistical properties of Mg II absorbers based on the halo occupation framework. The underlying assumption of the model is that all absorbers originate in the dark matter halos that host galaxies, and that the strength of an absorber is proportional to the amount of cold gas projected along the line

of sight through the halo. The two quantities that we specify in the model are (1) the mean absorption strength per unit surface gas mass density $A_W(M)$, and (2) the mean covering factor of the cold gas $\kappa_g(M)$. Both of these quantities are allowed to vary as a function of halo mass and together they determine the conditional probability distribution of W_r as a function of halo mass, $P(W_r|M)$.

For the conditional probability distribution function of equivalent widths, $P(W_r|M)$, the first quantity A_W determines how broad the distribution is, the second quantity κ_g governs the normalization of the PDF. In this statistical approach, we parameterize the physics that governs the gaseous halo and then allow the observational data to determine the best-fit values of the model. In this way, our approach is complementary to ab initio models for QSO absorption systems. The halo occupation of cold gas driven by the data can be compared to both analytic models and hydrodynamical simulations of cosmological structure growth.

We find that models in which the cold gas fraction varies smoothly with halo mass are not able to properly match either the frequency of absorbers or the observed anti-correlation between W_r and mean halo bias. Models that incorporate a rapid transition in the cold gas fraction—from low-mass halos that contain predominantly cold gas to high-mass halos that contain predominantly shock-heated gas and cannot contribute significantly to the observed Mg^+ absorption—accurately fit the observational data.

This latter model is consistent with the results of recent numerical simulations that display a revised picture in the mass assembly of galaxies (Birnboim & Dekel 2003; Kereš et al. 2005; Dekel & Birnboim 2006; Birnboim et al. 2007). The classical paradigm of galaxy formation states that all gas accreted onto the halo is shock heated at the virial radius and cooling begins at the inner regions of the halo. In the revised picture, shock heating does not occur in halos below a transitional mass scale, where the compression time is longer than the cooling time. Beyond the transitional mass, however, shock heating develops and becomes stable. In the revised scenario, gas *heating* occurs as an inside-out process until the entire halo is within the shock radius. But in high-mass halos that is dominated by a “hot-mode” accretion, some fraction of cold streams can still penetrate through the shock heated gas and reach the center of these halos.

In our analysis, we find a best-fit transitional mass scale of $M = 10^{11.5} h^{-1} M_\odot$, in excellent agreement with predictions from these numerical simulations. In addition, we constrain the cold gas fraction in high-mass halos to be $\sim 6\%$ relative to the cold gas fraction in the pre-shock regime. The best-fit model predicts that the majority of absorbers with $W_r \gtrsim 2 \text{ \AA}$ arise in the pre-shock mass regime, while lower- W_r systems are equally predominantly contributed by post-shock halos. In the following section, we discuss in more detail of the implications of these constraints in the transition halo model.

6.1. Covering Fraction of Cold Gas, κ_g

The four-point function κ_g presented in Figure 4a represents the integrated probability that a sight line through a halo yields an absorber. We note that this is governed by two physical quantities: the mean covering fraction of cold gas per halo and the fraction of halos that contain cold gas. Interpretations of the best-fit function must take these factors into account.

We find that κ_g increases rapidly with halo mass from being vanishingly small at $M \sim 10^{10} h^{-1} M_\odot$ to unity by $M \sim 10^{11.5}$

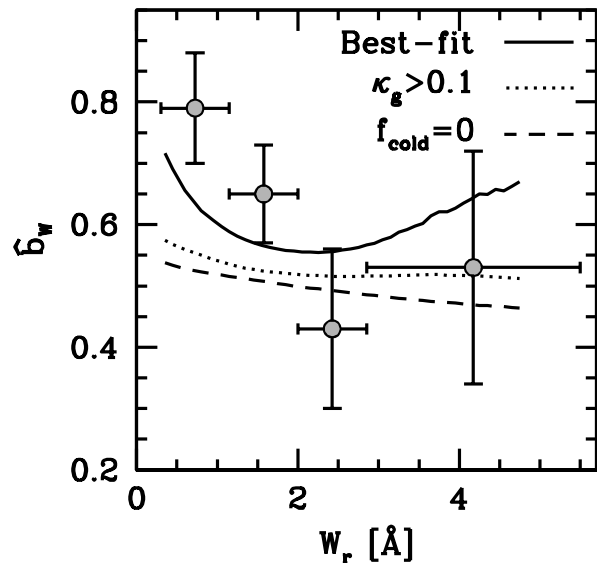


FIG. 7.— Relative bias \hat{b}_W as a function of W_r , demonstrating the significance of the constraints on the mean gas covering fraction at low masses and the cold gas fraction at high masses. The points are the B06 data, and the solid curve is the best-fit transition model from Figure 2 and Table 1. The dotted curve is the best-fit model adjusted such that $M < 10^{11} h^{-1} M_\odot$ halos have $\kappa_g = 0.1$. The dashed curve is the best-fit model with f_{cold} set to zero.

$h^{-1} M_\odot$, at the midpoint of the cold-hot phase transition (cf. Figure 4b). The strong constraints on the low-mass cutoff in κ_g are driven primarily by the bias data. Figure 7 compares the bias data (points) and best-fit transition model (solid curve) from Figure 2c with an additional model that demonstrate these constraints. The dotted curve is the bias produced when low-mass halos contribute significantly to the absorber statistics. This was calculated by adjusting the best-fit model such that the minimum value of κ_g is 0.1, while reducing the amplitude of κ_g at $M > 10^{11} h^{-1} M_\odot$ by $\sim 30\%$ to correctly match $f(W_r)$. A contribution from 10% of low-mass halos nearly washes out the anti-correlation, but more importantly lowers the overall bias of absorbers well below the measurements.

In the best fit model, the contribution at lower masses ($M \lesssim 10^{10.5}$) becomes negligible in order to match the clustering bias. The numerical models of accretion Dekel & Birnboim (2006) predict that the cold mode of accretion dominates in a range of halo masses rather than a single transition. Shock heating, which is efficient for massive halos, is also stable at $M \lesssim 10^{10} h^{-1} M_\odot$. Although the virial temperatures at these mass scales are low, efficient shock heating of halo gas in these halos could explain the dearth of absorbers at low masses at $z \sim 0.6$.

However, the model indicates a small contribution to the total absorbing cross section from $M \sim 10^{11} h^{-1} M_\odot$ halos. This can be interpreted as either these halos have on average a few percent covering fraction of warm/cold gas (producing the observed Mg II features), or a few percent of galaxies in these halos have extended Mg II gaseous halos. An unbiased galaxy– Mg II pair sample, established based on known galaxies along the lines of sight to background QSOs discussed in § 5.1, is necessary to break the degeneracy between the two

competing factors.

Tripp & Bowen (2005) have recently measured the incidence of Mg II absorption around galaxies to be $\sim 50\%$ out to $42 h^{-1} \text{ kpc}$ (physical) for a sample of objects within the redshift range $0.3-0.55$. This radius is roughly comparable to R_g for $10^{11.5} h^{-1} M_\odot$ halos, in the regime where $\kappa_g \approx 1$ in the best-fit model. The gas radius in the model scales as $M^{1/3}$, and will therefore change with the luminosity of the targeted galaxy. The range in luminosities of the Tripp & Bowen sample is 3 magnitudes, which probes nearly an order of magnitude in halo mass (see, e.g., the HOD analysis of SDSS and DEEP2 galaxy clustering data in Zheng et al. 2007). An incidence of less than unity is not surprising given the large search radius and luminosity spread in the Tripp & Bowen (2005) study. Given the distribution of galaxy luminosities in such a sample and a model for the halo occupation of *galaxies* at the proper redshifts, a quantitative comparison can be made and observational data on the incidence of absorption can be used to further constrain the models.

At $M > 10^{12} h^{-1} M_\odot$, where $R_{\text{sh}} = R_g$, the unity of κ_g indicate that all halos must contribute to the known Mg II statistics through the cold gas that survived the shocks. This explains the overall strong bias of absorbers measured in B06, i.e. the elevated mean bias is due to a significant contribution from high mass halos. B06 have interpreted the anti-correlation between W_r and M as due to predominant contribution to strong Mg II absorbers ($W_r > 2 \text{ \AA}$) from starburst outflows in low-mass systems. In our model, however, this anti-correlation results from high mass halos in the post-shock regime that have low cold gas fractions and can only contribute to $W_r \lesssim 1 \text{ \AA}$ absorbers.

Starbursts are not required to account for the mean mass of $W_r \sim 2 \text{ \AA}$ systems; absorption line with a width of 2 \AA implies at maximum velocity difference of $\sim 200 \text{ km s}^{-1}$ between individual components, which is less than twice the virial velocity of a $10^{11.5} h^{-1} M_\odot$ NFW halo, 220 km s^{-1} . Due to the high covering factors required to fit $f(W_r)$, in the starburst scenario nearly all halos of $10^{11.5-12} h^{-1} M_\odot$ would be experiencing an episode of star formation strong enough to push outflows to one third the virial radius. We note, however, that outflows are expected to be asymmetric, making it difficult to create high covering fractions through starbursting alone. Although rapidly star forming systems are likely to contribute to absorber statistics to some degree, it is not necessary to invoke a significant frequency of such systems to reproduce the observations.

6.2. Cold Gas in the Post-Shock Regime

The constraints on f_{cold} in the transition model are driven by a combination of the frequency and bias data. If cold gas is too abundant at high masses, then a \hat{b}_W - W_r anti-correlation cannot be produced (as expected from the results of the classical model) and the frequency distribution becomes tilted to higher W_r . The dashed curve in Figure 7 demonstrates the effect of having no cold gas in hot-mode halos by setting $f_{\text{cold}} = 0$. This weakens the \hat{b}_W - W_r anti-correlation has a strong effect on the overall bias scale of the absorbers.

In our model f_{cold} is independent of halos mass, thus a Milky-Way size halo, just outside the transition regime, is predicted to have only $\sim 6\%$ cold gas. Multiphase models of the gaseous halo by Maller & Bullock (2004) and Chelouche et al. (2007) predict high cold gas fractions ($\gtrsim 0.2$), but these predictions depend sensitively on the adopted cloud

size and are nearly an order of magnitude more than observational inventories of the cold gas in the Milky Way halo (Putman 2006). The simulations of Kereš et al. (2005) and Kravtsov (2003) (as analyzed in Birnboim et al. 2007) also imply $f_{\text{cold}} < 0.1$ for all halos $M > 10^{12} h^{-1} M_\odot$, but they do not have enough volume to address mass dependence of f_{cold} . With better bias data, it will be possible to add an additional degree of freedom in the model and make f_{cold} mass dependent.

Despite the poor constraints on the gas covering factor in the post-shock regime ($M > 10^{12.5} h^{-1} M_\odot$), it is clear the bias data are best fit by models with a high κ_g but a low cold gas fraction. At the cluster scale, $M \gtrsim 10^{14} h^{-1} M_\odot$, the virial temperature of such halos is too high to support significant amounts of low-ionization species. The situation at the group scale, $10^{13-14} h^{-1} M_\odot$, is less clear. The simulations of Kereš et al. (2005) and Birnboim et al. (2007) do not have sufficient volume to probe this mass scale. A relevant question is whether the two-phase medium of Mo & Miralda-Escude (1996) and Maller & Bullock (2004) can exist at these halo masses. These authors demonstrate that cold clouds can survive in massive halos, if these clouds are massive themselves. Dekel & Birnboim (2007) propose that accreted cold clouds in massive halos can also be long-lived. Observational searches for cold gas clouds in poor galaxy groups have yielded null detections (Zabludoff 2003), although the large-scale bias of Mg II absorbers requires that some fraction of absorbers exist at this mass scale. Some cold gas in group and cluster-sized halos should be associated with the satellite galaxies contained within it, but the covering fraction of these satellites is likely much less than unity.

Recent clustering measurements of Ly α absorbers by Ryan-Weber (2006) also yield a bias consistent with $\sim 10^{14} h^{-1} M_\odot$ halos. The cross-correlation function between LRGs and absorbers itself can directly address this question. If pairs exist at separations less than $1 h^{-1} \text{ Mpc}$, then it demonstrates that massive galaxies and cold gas exist in the same halo. The cross-correlation measurements of Bouché et al. (2004) show a signal at these small separations, but the significance of the detection is low and should be verified with a larger statistical sample.

6.3. Toward Understanding the Origin of Mg II Absorbers

We have demonstrated both that the halo-based approach can accurately model the data and that the parameters of the model can be well-constrained with those data. More concrete physical inferences about the distribution of cold gas in halos and its implications require several improvements to the model and the data in forthcoming studies.

Our analysis also demonstrates that the statistics of Mg II absorbers can be modeled by a representative sample of the dark halo population. The high incidence and covering factors required to fit the data imply that QSO absorbers are a ubiquitous phenomenon of the overall galaxy population. Galaxy-absorber pairs are not skewed to a special subset of the galaxy population, such as starburst systems, or biased to halos in a specific environment.

Additional data, such as an unbiased sample of galaxy-absorber pairs, the line-of-sight autocorrelation of absorbers, and the correlations between W_r and associated galaxy properties will allow better constraints in the model. Quantifying the relationship between cold gas and dark matter halos is a key step in painting a more complete picture of galaxy formation. By tracking the baryons that do not shine, the infor-

mation obtainable through this approach is complementary to that provided by observations of the galaxies themselves.

It is a pleasure to thank A. Kravtsov and B. Robertson for important discussions during the development of this project, and D. Weinberg for helpful comments on

an earlier version of this paper. The authors thank J. Prochaska for providing updated measurements on the Mg II frequency distribution function measurements prior to publication. J.L.T. and H.-W.C. were partially supported by NASA grant NNG06GC36G and NSF grant AST-0607510.

REFERENCES

- Abazajian, K., e. 2005, *AJ*, 129, 1755
 Bahcall, J. N. & Spitzer, L. J. 1969, *ApJ*, 156, L63+
 Bergeron, J. 1986, *A&A*, 155, L8
 Bergeron, J. & Boissé, P. 1991, *A&A*, 243, 344
 Bergeron, J. & Stasinska, G. 1986, *A&A*, 169, 1
 Berlind, A. A. & Weinberg, D. H. 2002, *ApJ*, 575, 587
 Birnboim, Y. & Dekel, A. 2003, *MNRAS*, 345, 349
 Birnboim, Y., Dekel, A., & Neistein, E. 2007, *MNRAS*, submitted, (astro-ph/0703435)
 Bouché, N., Murphy, M. T., & Péroux, C. 2004, *MNRAS*, 354, L25
 Bouché, N., Murphy, M. T., Péroux, C., Csabai, I., & Wild, V. 2006, *MNRAS*, 371, 495
 Bullock, J. S., Kolatt, T. S., Sigad, Y., Somerville, R. S., Kravtsov, A. V., Klypin, A. A., Primack, J. R., & Dekel, A. 2001, *MNRAS*, 321, 559
 Chelouche, D., Ménard, B., Bowen, D. V., & Gnat, O. 2007, submitted to *ApJ*, (astro-ph/0706.4336), 706
 Churchill, C. W., Mellon, R. R., Charlton, J. C., Jannuzi, B. T., Kirhakos, S., Steidel, C. C., & Schneider, D. P. 2000, *ApJS*, 130, 91
 Churchill, C. W. & Vogt, S. S. 2001, *AJ*, 122, 679
 Cooray, A. 2006, *MNRAS*, 365, 842
 Davé, R., Hernquist, L., Katz, N., & Weinberg, D. H. 1999, *ApJ*, 511, 521
 Dekel, A. & Birnboim, Y. 2006, *MNRAS*, 368, 2
 —. 2007, submitted to *MNRAS*, (astro-ph/0707.1214), 707
 Hamann, F. 1997, *ApJS*, 109, 279
 Kacprzak, G. G., Churchill, C. W., Steidel, C. C., Murphy, M. T., & Evans, J. L. 2007, submitted, (astro-ph/0703377)
 Kereš, D., Katz, N., Weinberg, D. H., & Davé, R. 2005, *MNRAS*, 363, 2
 Kravtsov, A. V. 2003, *ApJ*, 590, L1
 Lanzetta, K. M. & Bowen, D. 1990, *ApJ*, 357, 321
 Lu, L. & Wolfe, A. M. 1994, *AJ*, 108, 44
 Maller, A. H. & Bullock, J. S. 2004, *MNRAS*, 355, 694
 Mo, H. J. & Miralda-Escude, J. 1996, *ApJ*, 469, 589
 Murphy, M. T., Curran, S. J., Webb, J. K., Ménager, H., & Zych, B. J. 2007, *MNRAS*, 376, 673
 Navarro, J. F., Frenk, C. S., & White, S. D. M. 1997, *ApJ*, 490, 493
 Nestor, D. B., Turnshek, D. A., & Rao, S. M. 2005, *ApJ*, 628, 637
 Nestor, D. B., Turnshek, D. A., Rao, S. M., & Quider, A. M. 2007, *ApJ*, 658, 185
 Petitjean, P. & Bergeron, J. 1990, *A&A*, 231, 309
 Prochaska, J. X., Castro, S., & Djorgovski, S. G. 2003, *ApJS*, 148, 317
 Prochter, G. E., Prochaska, J. X., & Burles, S. M. 2006, *ApJ*, 639, 766
 Putman, M. E. 2006, *ApJ*, 645, 1164
 Rao, S. M., Turnshek, D. A., & Nestor, D. B. 2006, *ApJ*, 636, 610
 Rauch, M. 1998, *ARA&A*, 36, 267
 Ryan-Weber, E. V. 2006, *MNRAS*, 367, 1251
 Scoccimarro, R., Sheth, R. K., Hui, L., & Jain, B. 2001, *ApJ*, 546, 20
 Seljak, U. 2000, *MNRAS*, 318, 203
 Spitzer, L. J. 1956, *ApJ*, 124, 20
 Steidel, C. C. 1993, in *Astronomical Society of the Pacific Conference Series*, Vol. 49, *Galaxy Evolution. The Milky Way Perspective*, ed. S. R. Majewski, 227+
 Steidel, C. C. 1995, in *QSO Absorption Lines, Proceedings of the ESO Workshop Held at Garching, Germany, 21 - 24 November 1994*, edited by Georges Meylan. Springer-Verlag Berlin Heidelberg New York. Also *ESO Astrophysics Symposia*, 1995., p.139, ed. G. Meylan, 139+
 Steidel, C. C., Dickinson, M., Meyer, D. M., Adelberger, K. L., & Sembach, K. R. 1997, *ApJ*, 480, 568
 Steidel, C. C., Dickinson, M., & Persson, S. E. 1994, *ApJ*, 437, L75
 Steidel, C. C. & Sargent, W. L. W. 1992, *ApJS*, 80, 1
 Sternberg, A., McKee, C. F., & Wolfire, M. G. 2002, *ApJS*, 143, 419
 Tinker, J. L. 2007, *MNRAS*, 374, 477
 Tinker, J. L., Conroy, C., Norberg, P., Patiri, S. G., Weinberg, D. H., & Warren, M. S. 2007, *ApJ*, submitted, (astro-ph/0707.3445)
 Tinker, J. L., Weinberg, D. H., Zheng, Z., & Zehavi, I. 2005, *ApJ*, 631, 41
 Tripp, T. M. & Bowen, D. V. 2005, in *IAU Colloq. 199: Probing Galaxies through Quasar Absorption Lines*, ed. P. Williams, C.-G. Shu, & B. Menard, 5–23
 van den Bosch, F. C., Mo, H. J., & Yang, X. 2003a, *MNRAS*, 345, 923
 van den Bosch, F. C., Yang, X., & Mo, H. J. 2003b, *MNRAS*, 340, 771
 van den Bosch, F. C., Yang, X., Mo, H. J., Weinmann, S. M., Macciò, A. V., More, S., Cacciato, M., Skibba, R., & Kang, X. 2007, *MNRAS*, 376, 841
 Wang, B. 1993, *ApJ*, 415, 174
 Warren, M. S., Abazajian, K., Holz, D. E., & Teodoro, L. 2006, *ApJ*, 646, 881
 Wechsler, R. H., Zentner, A. R., Bullock, J. S., Kravtsov, A. V., & Allgood, B. 2006, *ApJ*, 652, 71
 White, M., Zheng, Z., Brown, M. J. I., Dey, A., & Jannuzi, B. T. 2007, *ApJ*, 655, L69
 White, S. D. M. & Frenk, C. S. 1991, *ApJ*, 379, 52
 Wolfe, A. M., Gawiser, E., & Prochaska, J. X. 2005, *ARA&A*, 43, 861
 Yang, X., Mo, H. J., & van den Bosch, F. C. 2003, *MNRAS*, 339, 1057
 Zabludoff, A. I. 2003, in *Astrophysics and Space Science Library*, Vol. 281, *The IGM/Galaxy Connection. The Distribution of Baryons at z=0*, ed. J. L. Rosenberg & M. E. Putman, 291+
 Zheng, Z., Coil, A. L., & Zehavi, I. 2007, *ApJ*, submitted, (astro-ph/0703457)
 Zheng, Z. & Weinberg, D. H. 2007, *ApJ*, 659, 1
 Zibetti, S., Ménard, B., Nestor, D., & Turnshek, D. 2005, *ApJ*, 631, L105